



## Full length article

# Anisotropic dynamic response of AlSi10Mg fabricated via laser powder bed fusion under plate impact

N.B. Zhang <sup>a</sup>, K. Yang <sup>c</sup>, Y.C. Li <sup>a</sup>, Z.H. Lin <sup>a</sup>, Y. Cai <sup>b</sup>, H.W. Chai <sup>a,\*</sup>, H.L. Xie <sup>d</sup>, L. Lu <sup>a</sup>, S.N. Luo <sup>a</sup>

<sup>a</sup> Materials Dynamics Data Science Center, School of Materials Science and Engineering, Southwest Jiaotong University, Chengdu, Sichuan, PR China

<sup>b</sup> The Peac Institute of Multiscale Sciences, Chengdu, Sichuan, PR China

<sup>c</sup> School of Materials Science and Engineering, Taiyuan University of Science and Technology, Taiyuan, Shanxi, PR China

<sup>d</sup> Shanghai Synchrotron Radiation Facility, Shanghai Advanced Research Institute, Chinese Academy of Sciences, Shanghai, PR China

## HIGHLIGHTS

- The SLM-fabricated AlSi10Mg exhibits an anisotropic microstructure.
- The HEL for TD samples is about 40% higher than that along BD, given the initial  $\langle 100 \rangle \parallel$ BD texture.
- Spall strength for loading along TD is about 18% higher than that along BD.
- Melt pool morphology leads to interpool and intrapool fracture modes for loading along BD and TD, respectively.

## ARTICLE INFO

## Keywords:

AlSi10Mg alloy

Laser powder bed fusion

Spall strength

Anisotropy

## ABSTRACT

The effects of structural anisotropy on dynamic yield and spallation damage of an AlSi10Mg alloy manufactured via laser powder bed fusion are investigated via plate impact experiments along the build direction (BD) and the transverse direction (TD). Free surface velocity histories are measured to deduce its dynamic mechanical properties. The as-received and postmortem samples are characterized with scanning electron microscopy, metallographic microscopy, electron backscatter diffraction and synchrotron X-ray computed tomography. The Hugoniot elastic limit for loading along TD is about 40% higher than that along BD, given the initial  $\langle 100 \rangle \parallel$ BD texture. For spallation, voids prefer to nucleate at melt pool boundaries. Spall strength for loading along TD is about 18% higher than that along BD, as a result of higher critical stress for void nucleation and less nucleation sites due to the melt pool morphology. The damage evolution features are also correlated well with melt pool morphology and grain morphology within the pool interior, demonstrating the “ductile” interpool and “brittle” intrapool fracture modes for loading along BD and TD, respectively.

## 1. Introduction

Additive manufacturing (AM) or three-dimensional (3D) printing is a breakthrough in manufacture and can produce complex engineering parts for medical, aerospace, and automotive applications [1–4]. Among the available additive manufacturing processes, Laser Powder Bed Fusion (L-PBF) has received significant attention owing to its advantages of free-forming design, material flexibility, short production cycle and relative low production costs [5–8].

AlSi10Mg, an Al-based hypoeutectic alloy, is presently the most common aluminum alloy used in the L-PBF-based industries [9–13]. Numerous studies have been dedicated to microstructure characterization and mechanical response [14–21]. AlSi10Mg processed by L-PBF exhibits higher yield stress and ultimate tensile strength than the cast or heat-treated counterparts under quasi-static loading [22–29]. Since the

L-PBF manufacture involves fast melting and solidification of powder by scanning laser beam, the typical microstructure of L-PBF-fabricated AlSi10Mg consists of overlapping melt pools [30,31].

L-PBF fabricated AlSi10Mg has been widely reported to exhibit anisotropic tensile properties [32–37]. Generally, When loading perpendicular to the building direction, AlSi10Mg exhibit superior yield strength and elongation to fracture. While higher strain hardening capacity and consequently higher ultimate tensile strength are observed for loading along the building direction [19]. Strain-rate sensitivity and anisotropy in dynamic mechanical response relative to the build direction (or melt pools) were investigated with split Hopkinson pressure bars [29,38–44]. When subjected to strain rates within 1000–3000 s<sup>-1</sup>, AlSi10Mg showed a pronounced dependence of dynamic properties on the build orientation. However, this anisotropy was

\* Corresponding author.

E-mail address: [hwchai@swjtu.edu.cn](mailto:hwchai@swjtu.edu.cn) (H.W. Chai).

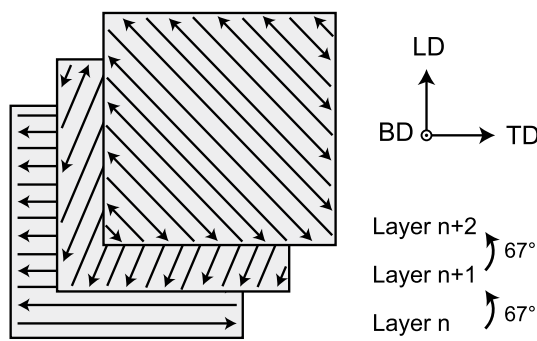


**Fig. 1.** Illustration of the L-PBF-fabrication strategy consisting of intralayer line scanning and interlayer rotation. BD: build direction; LD: longitudinal direction; TD: transverse direction.

absent for strain rates outside this range [41]. In addition, thermal softening was observed in dynamically tested AlSi12 samples at elevated temperatures [42].

Given the potential applications of L-PBF-fabricated AlSi10Mg in aerospace, automotive and marine industries, several studies were dedicated to the Hugoniot equation of state (EOS) [45] and spallation damage [46,47] of L-PBF-fabricated AlSi10Mg. Previous plate impact experiments demonstrated superior Hugoniot elastic limit (HEL) and spall strength of L-PBF-fabricated AlSi10Mg over those of cast AlSi10Mg (increase by factors of two and four, respectively). With increasing tensile strain rate, the fracture mode changed from ductile to brittle [46]. Laser-driven experiments showed that the fabrication parameters had a strong influence on the HEL [47]. Despite the complex anisotropic microstructure in L-PBF-fabricated AlSi10Mg, no significant anisotropy was observed in HEL and spall strength [45–47]. Considering the considerable amount of pore flaws inherited from L-PBF (e.g., a 2.25% porosity was seen in the laser-driven L-PBF samples [47]), one open question is whether the effect of microstructural anisotropy is outrun by that of the pre-existing pore flaws. Overall, the structure-property relation is still under explored for L-PBF-fabricated AlSi10Mg. Since AlSi10Mg alloys exhibit anisotropic mechanical properties under quasi-static compression and split Hopkinson pressure bar loading, with anisotropic structure in nature, anisotropic dynamic responses should exist under higher strain rate loading based on the afore-established understanding. Moreover, as a complement to scanning electron microscopy and metallographic microscopy, micro X-ray computed tomography (XCT) [48–50] can characterize the three-dimensional (3D) internal structure features, and provide more details about the preexisting pores and damage characteristics of L-PBF-fabricated AlSi10Mg.

In this study, plate impact experiments are conducted on an L-PBF-fabricated AlSi10Mg alloy along two different directions, the build direction (BD) and the transverse direction (TD), to investigate the effect of structure anisotropy on dynamic yield and spallation damage. Free-surface velocity histories are measured to derive HEL (yield strength) and spall strength (resistance to high-rate tensile loading). Scanning electron microscope (SEM), optical microscopy, electron back-scattering diffraction (EBSD), and XCT are conducted to obtain spatial distributions and morphologies of voids or cracks. The connections between anisotropic mechanical properties and microstructure features inherent from the additive manufacture are established. Based on the experimental observations, TD samples own higher HEL and spall strength. Thus, for component manufacturing or part repairment in spacecraft and aircraft structures, the material performance can be improved by adjusting the scanning direction.

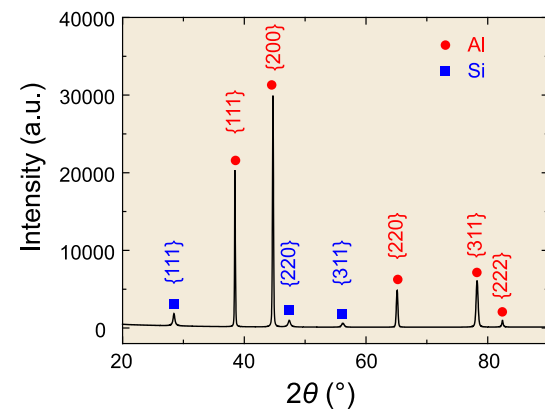


**Fig. 2.** X-ray diffraction pattern of the L-PBF-fabricated AlSi10Mg sample obtained with a Cu  $K_{\alpha}$  source.  $2\theta$ : diffraction angle.

## 2. Materials and experiments

### 2.1. Materials

The L-PBF-fabricated AlSi10Mg alloy used in this study is commercially produced by Xi'an Bright Laser Technologies Co., Ltd. A cuboid-shaped block with dimensions of 18 mm (BD: build direction)  $\times$  40 mm (TD: transverse direction)  $\times$  40 mm (LD: longitudinal direction) is fabricated from pre-alloyed AlSi10Mg powder (nominal content, in wt.-%: 9.82% Si, 0.29% Mg, 0.09% Fe and Al in balance) with particle size ranging from 15 to 53  $\mu\text{m}$  within an argon atmosphere. Other fabrication parameters are AM machine type: BLT-S210, laser power: 320 W, spot size: 0.1 mm, line scanning speed: 1300  $\text{mm s}^{-1}$ , line spacing:  $\sim 0.12$  mm and build-platform temperature: 35 °C. The interlayer rotation scheme is illustrated in Fig. 1: each layer,  $\sim 30 \mu\text{m}$  thick, is rotated by 67° with respect to its preceding layer. After fabrication, the L-PBF-fabricated AlSi10Mg alloy are subjected to T5 heat treatment (for stress relief) at 300 °C for 2 h.

The microstructures of initial and postmortem samples are characterized via X-ray diffraction (XRD), scanning electron microscopy (SEM), electron backscatter diffraction (EBSD) and X-ray computed tomography (XCT). XRD is conducted with a Panalytical Empyrean X-ray diffractometer with Cu- $K_{\alpha}$  radiation (0.15405-nm wavelength). Metallographic characterization is performed with an Olympus SZ61 optical microscope. SEM and EBSD characterizations are performed with an FEI Quanta 250 FEG-SEM equipped with Oxford EDS or EBSD detectors. In addition, XCT experiments are performed at beamline BL16U2 of the Shanghai Synchrotron Radiation Facility (SSRF) with a voxel size of about 1.6  $\mu\text{m}$ .

The XRD pattern of the L-PBF-fabricated AlSi10Mg alloy (Fig. 2) reveals the typical face-centered cubic (FCC) Al matrix and the eutectic Si phase. During rapid cooling in the L-PBF process, the element Si is supersaturated and then evolves in precipitates in the Al matrix [51]. The EBSD analysis indicates a significant structural anisotropy. The anisotropic microstructure throughout the melt pools can be explained by non-steady solidification behavior. The differences of growth rate and thermal gradient at the melt pool border or in the melt pool interior during solidification lead to distinct solidification structure morphologies between internal and peripheral melt pool regions [52]. The grains follow a bimodal size distribution, consisting of coarse columnar grains and fine equiaxed grains (Fig. 3a and b). Solidification generally proceeds along the direction of heat flow, i.e., along the  $\langle 100 \rangle$  orientation of AlSi10Mg [53], leading to coarse columnar grains elongated in the build direction or the  $\langle 100 \rangle$  orientation (Fig. 3c and d). In addition, the melt pools form with a “fish scale” morphology inherited from the L-PBF process (Fig. 3e). The melt pool structures come from solidification of melted material induced by a moving

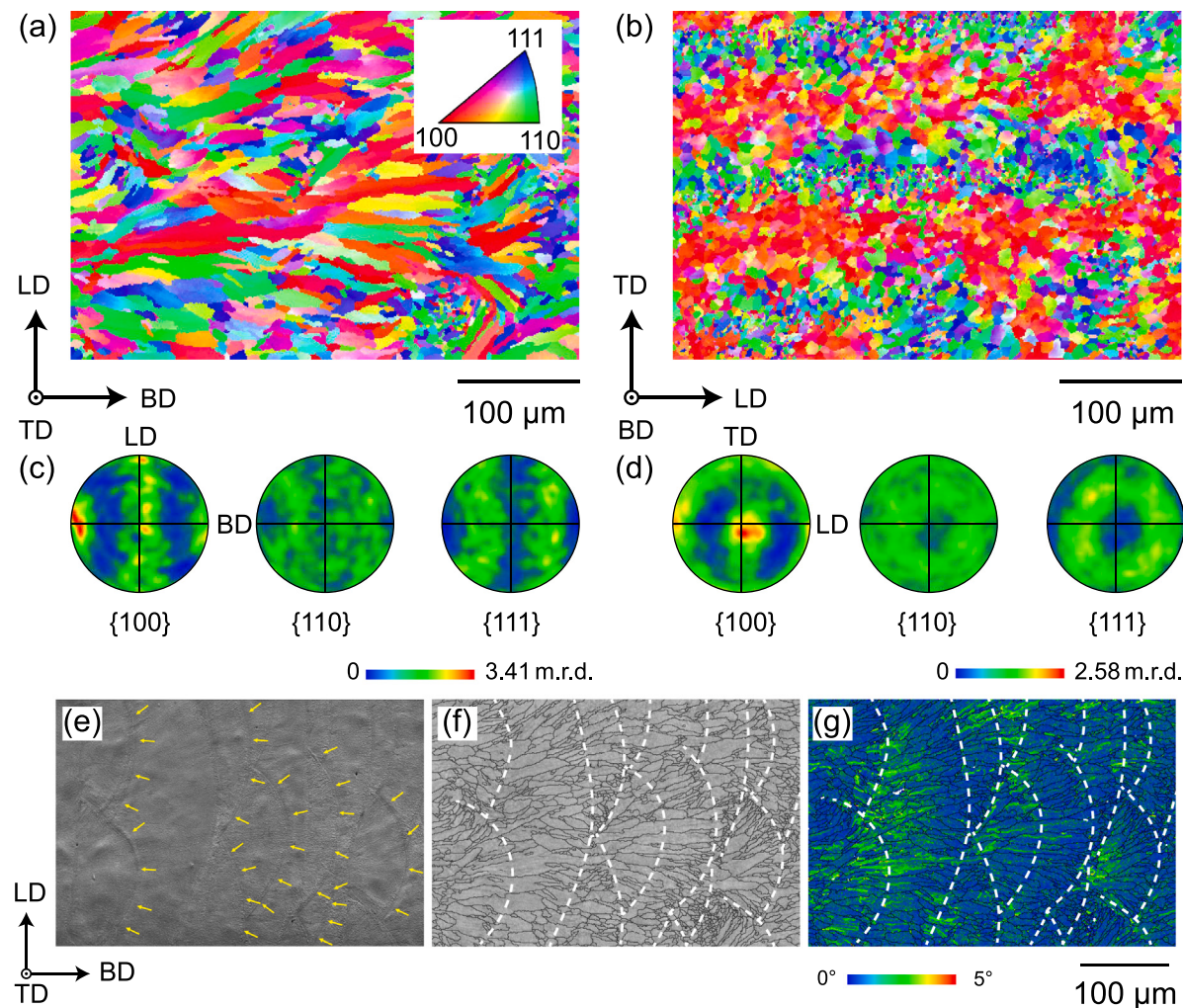


**Fig. 3.** EBSD characterization of the L-PBF-fabricated AlSi10Mg sample. (a, b) Inverse pole figure (IPF) map and (c,d) corresponding pole figures for the LD-BD plane and the TD-LD plane, respectively. (e) SEM micrograph, (f) corresponding band-contrast map and (g) kernel average misorientation (KAM) map for the LD-BD plane. The melt pool boundaries (MPBs) are marked by the yellow arrows in (e) and the white dashed lines in (f) and (g).

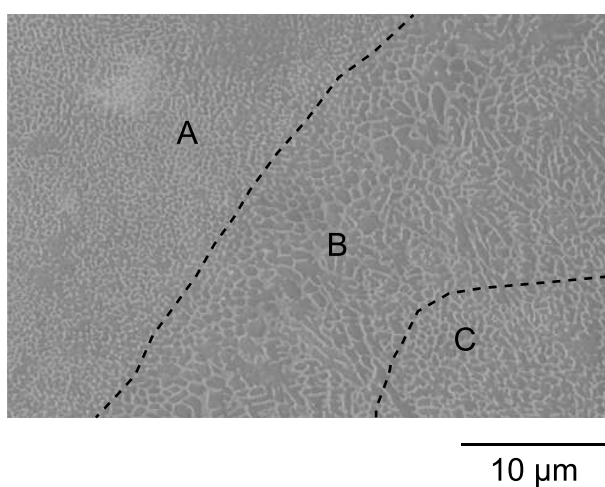


**Fig. 4.** SEM micrograph of the LD-TD plane of the L-PBF-fabricated AlSi10Mg sample.

heating source [33]. Their size and arrangement is highly dependent on scan strategy [19]. The coarse columnar grains are more likely to appear in the melt pool interior, while the fine equiaxed grains,

at the melt pool boundaries (MPBs) in Fig. 3f. The higher-resolution SEM image of the LD-TD plane (Fig. 4) shows Al cells decorated with continuous networks of eutectic Si [7,54]. Moreover, the ultrafine Al cells are coarser near the MPBs (area B in Fig. 4) than those in melt pool interiors (area A and C in Fig. 4) due to partial re-melting during deposition of a top layer [55].

## 2.2. Plate impact experiments

The initial density ( $\rho_0$ ) is measured with the Archimedean method and the longitudinal ( $C_L$ ) and transverse sound ( $C_T$ ) velocities are obtained with the ultrasound method. The Poisson's ratio ( $\nu$ ) and bulk sound speed ( $C_B$ ) are calculated from  $C_L$  and  $C_T$  [56]. All sound velocities and Poisson's ratio along BD and TD are summarized in Table 1. The L-PBF-fabricated AlSi10Mg used in this study achieves a density of 99.3% of the theoretical maximum density.

Plate impact experiments are conducted on a single-stage gas gun (Fig. 5a and b). Before experiments, both surfaces of the 2024-T4 Al alloy flyer plates and L-PBF-fabricated samples are polished to mirror finish. A flyer plate (4) is attached to a low polycarbonate sabot (3) with a recess (10), and accelerated in the gun barrel (1) by the high pressure gas. The flyer plate speed is measured with a magnetic induction system (2) within 0.5%. A momentum trap ring (6) made of the 2024-T4 Al alloy is implemented to minimize the release wave effect [57,58]. After impact, AlSi10Mg samples (5) are “soft-recovered” with soft materials

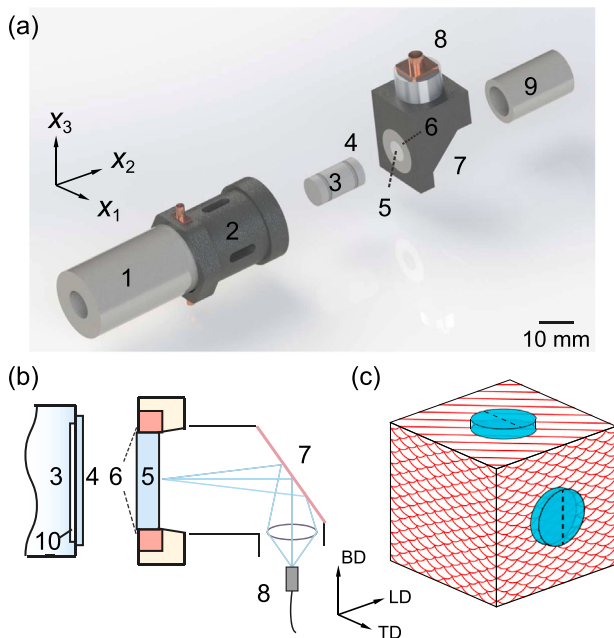


**Fig. 5.** (a,b) Schematic setups for plate impact experiments. 1: gun barrel; 2: magnetic induction velocimeter; 3: polycarbonate sabot; 4: flyer plate; 5: sample; 6: momentum trap ring; 7: thin-film mirror; 8: lens with the optical fiber connected to a laser Doppler velocimeter; 9: recovery cylinder; 10: recess for release waves. (c) Illustration of the loading orientations in the sample coordinate system (BD-TD-LD).

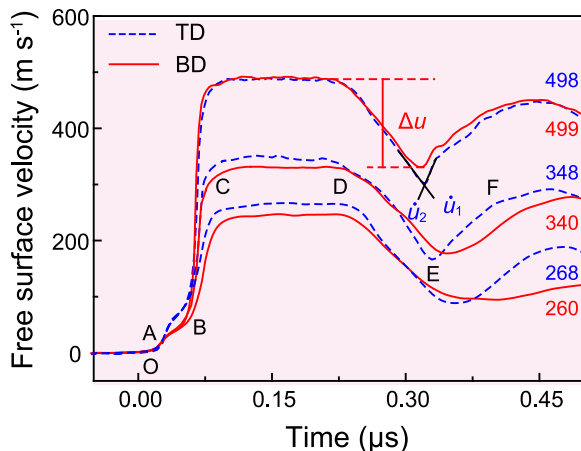


**Fig. 6.** Free surface velocity histories,  $u_{fs}(t)$ , for loading along TD and BD at different impact velocities as noted on each curve (in  $m s^{-1}$ ).

in the recovery cylinder (9) for subsequent microstructure characterizations. The free surface velocity ( $u_{fs}$ ) of AlSi10Mg is measured with a lens-coupled laser Doppler velocimeter (8) (LDV) which is similar to a photon Doppler velocimetry [59,60]. The whole experimental system with stable and controllable impact velocity within  $10 m s^{-1}$  and impact angle less than  $10 mrad$  [61] makes sure the reliability and consistency of the obtained results.

To investigate the effects of microstructural anisotropy, the samples are impact-loaded along BD and TD. For simplicity, these two kinds of samples are referred to as the BD and TD samples, respectively. Disk-shaped samples with different orientations are harvested from the AlSi10Mg block following the scheme illustrated in Fig. 5c. Flyer plates and samples are of a disk shape with a diameter of  $13.20 \pm 0.01$  mm and  $10.00 \pm 0.01$  mm, respectively. The thicknesses for each shot are summarized in Table 2.

**Table 1**

Summary of material parameters for the BD- and TD-loading samples.  $\rho_0$ : initial density;  $C_L$ : longitudinal sound speed;  $C_T$ : transverse sound speed;  $C_B$ : bulk sound speed;  $\nu$ : Poisson's ratio.

Sample type	$\rho_0$ (g cm $^{-3}$ )	$C_L$ (km s $^{-1}$ )	$C_T$ (km s $^{-1}$ )	$C_B$ (km s $^{-1}$ )	$\nu$
BD	2.65	6.65	3.38	5.38	0.32
TD	2.65	6.64	3.32	5.42	0.32

### 3. Results

#### 3.1. Free surface velocity analysis

Totally, six shots are carried out at three fixed impact velocities along BD or TD, and the corresponding free surface velocity histories,  $u_{fs}(t)$ , are shown in Fig. 6. For each fixed impact velocity, since the variations are within  $10 m s^{-1}$ , there are negligible influences on comparison between the BD and TD samples. Typical elastic-plastic two-wave structures with the elastic precursor (OA), the plastic shock (BC), the shock plateau (CD), the release (DE) from the recess behind the flyer plate, and the spall pullback (EF) are shown in Fig. 6. The interaction of the release fan from the flyer plate free surface with that reflected from the sample free surface induces tension in the sample interior. When this tensile stress exceeds the critical stress of the sample, spallation occurs. The details of wave propagation and interaction for spallation can be found elsewhere [62].

The point on the shock Hugoniot at which a material transitions from a purely elastic state to an elastic-plastic state is called the Hugoniot elastic limit (HEL, point A in Fig. 6). The stress at the HEL is calculated as

$$\sigma_{HEL} = \rho_0 u_{p1} u_{s1}. \quad (1)$$

The particle velocity ( $u_{p1}$ ) of the elastic precursor is approximately equal to half of the free surface velocity at HEL. The elastic wave velocity ( $u_{s1}$ ) is approximately equal to the longitudinal sound velocity at ambient condition, i.e.,  $C_L$ . The  $\sigma_{HEL}$  values are 0.32 and 0.45 GPa for the BD and TD samples, respectively. The yield stress follows as

$$\sigma_y = \frac{1 - 2\nu}{1 - \nu} \sigma_{HEL}. \quad (2)$$

The  $\sigma_y$  values for the BD and TD samples are 0.17 and 0.24 GPa, respectively.

Via the impedance match method [63] with known projectile velocity ( $u_p$ ) and the Hugoniot equations of state for the 2024-T4 Al alloy [64] and the L-PBF-fabricated AlSi10Mg sample [45], the peak shock stress ( $\sigma_H$ ) is obtained as

$$\sigma_H = \sigma_{HEL} + \frac{\rho_0 u_{s1}}{u_{s1} - u_{p1}} \left( C_0 + \lambda u_{p2} - u_{p1} \right) \left( u_{p2} - u_{p1} \right), \quad (3)$$

$C_0$  and  $\lambda$  are known material parameters [45].  $u_{p2}$  and  $u_{s2}$  are particle velocity and shock wave velocity of the plastic wave, respectively.

Spall strength ( $\sigma_{sp}$ ) is estimated from  $u_{fs}(t)$  with the acoustic method [65,66] as

$$\sigma_{sp} \approx \rho_0 C_L \Delta u \frac{1}{1 + \frac{C_L}{C_B}}. \quad (4)$$

Since the magnitude of tension pulse is attenuated as it propagates to the sample free surface, an underestimated spall strength is calculated from  $u_{fs}(t)$  via Eq. (4). Thus, we also introduce [65,67]

$$\sigma_{sp}^* \approx \frac{1}{2} \rho_0 C_B (\Delta u + \delta), \quad (5)$$

with

$$\delta \approx \left( \frac{h_s}{C_B} - \frac{h_s}{C_L} \right) \frac{\dot{u}_1 \dot{u}_2}{\dot{u}_1 + \dot{u}_2}. \quad (6)$$

Here, pullback velocity  $\Delta u = u_{fs,D} - u_{fs,E}$ ,  $h_s$  is the thickness of the spalled layer directly obtained from an SEM micrograph.

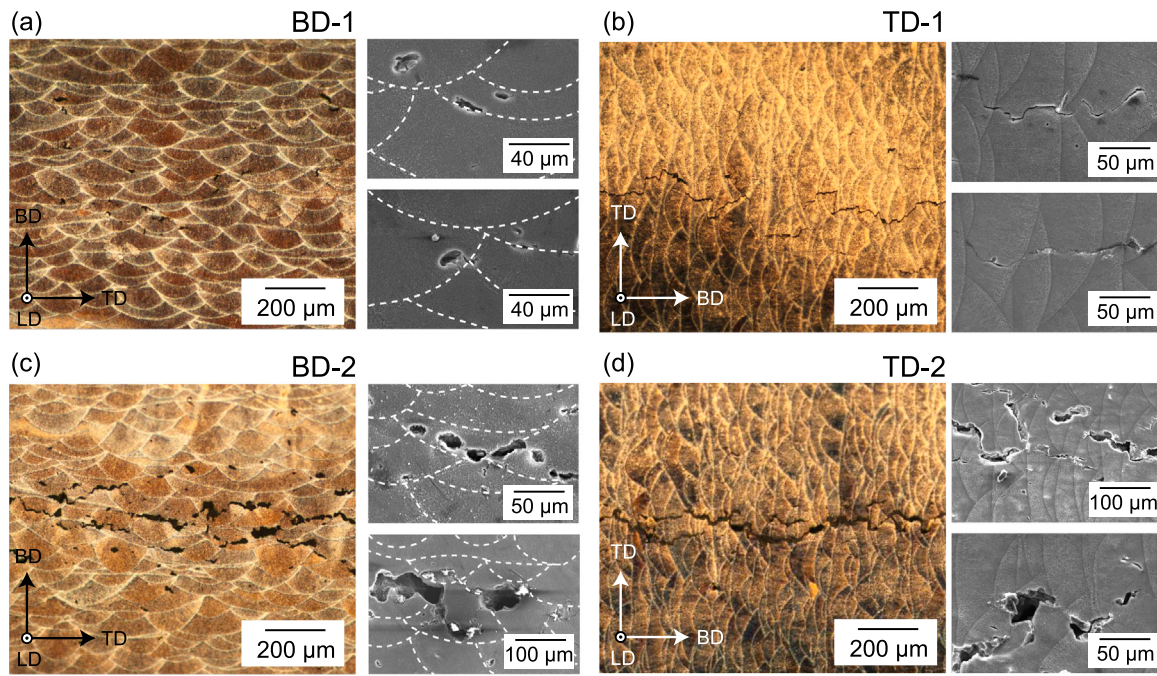


Fig. 7. Metallographs or SEM images of the cross-sections for the postmortem samples from shots (a) BD-1, (b) TD-1, (c) BD-2 and (d) TD-2.

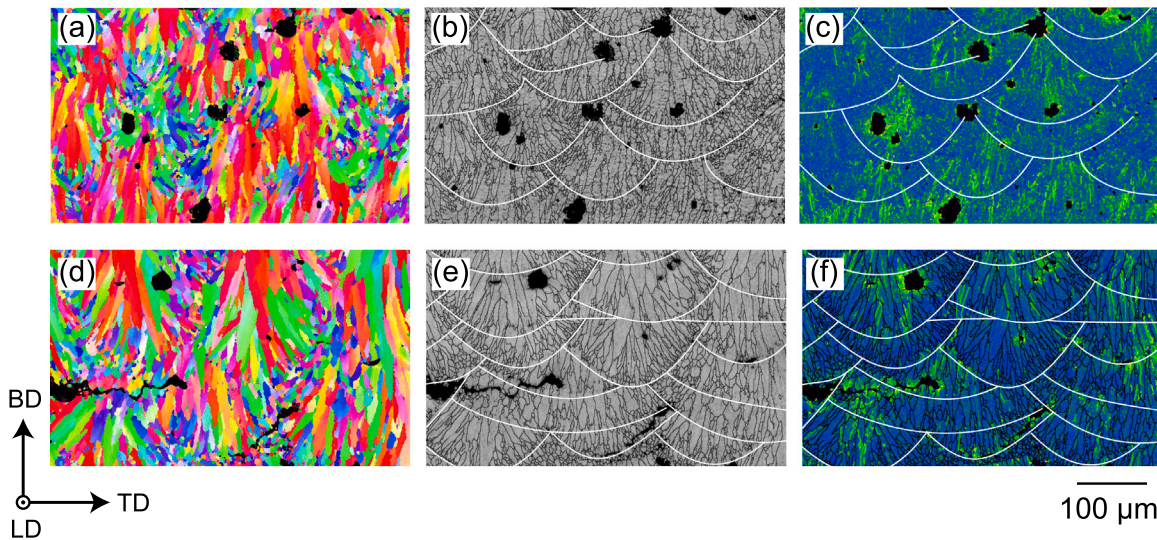
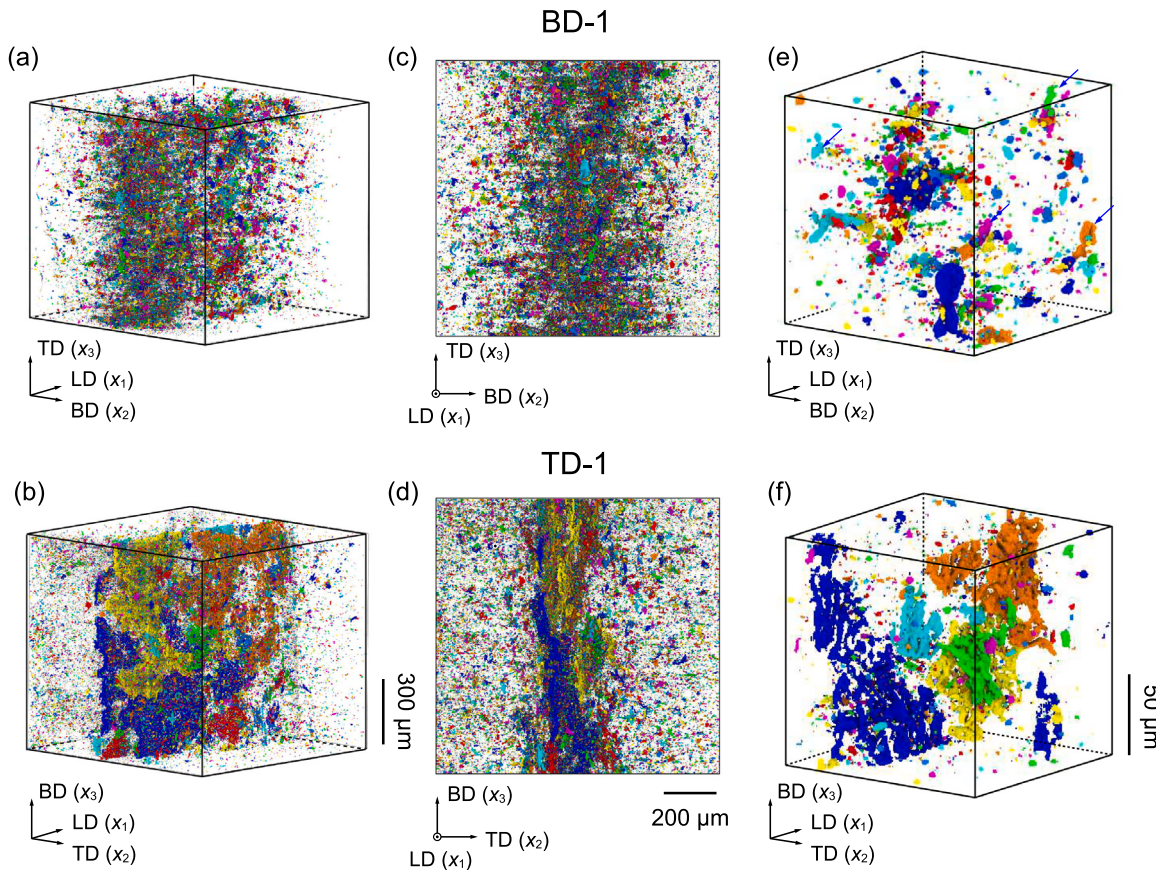


Fig. 8. EBSD characterizations of two typical spallation regions for shot BD-1. (a, d) IPF maps, corresponding (b, e) band-contrast maps and (c, f) KAM maps for the BD-TD plane. Shock direction: top to bottom.

Table 2

Summary of experimental parameters and results for the spallation experiments.  $d_f$ : flyer plate thickness;  $d_s$ : sample thickness;  $u_f$ : flyer plate velocity;  $\sigma_{\text{HEL}}$ : stress at Hugoniot elastic limit;  $\sigma_H$ : peak shock stress;  $\tau$ : pulse duration;  $\dot{\epsilon}$ : tensile strain rate;  $\Delta u$ : pullback velocity;  $\sigma_{\text{sp}}$ : spall strength;  $\sigma_{\text{sp}}^*$ : spall strength (considering the effect of spall plane position);  $\dot{u}_2$ : re-acceleration. Numbers in parentheses denote uncertainties in the last 1 or 2 digits.

Shot No.	$d_f$ (mm)	$d_s$ (mm)	$u_f$ ( $\text{m s}^{-1}$ )	$\sigma_{\text{HEL}}$ (GPa)	$\sigma_H$ (GPa)	$\tau$ (μs)	$\dot{\epsilon}$ ( $10^5 \text{ s}^{-1}$ )	$\Delta u$ ( $\text{m s}^{-1}$ )	$\sigma_{\text{sp}}$ (GPa)	$\sigma_{\text{sp}}^*$ (GPa)	$\dot{u}_2$ ( $10^8 \text{ m s}^{-2}$ )
BD-1	0.752 (2)	1.496 (2)	260 (5)	0.32 (1)	1.92 (1)	0.14 (1)	0.86 (1)	150 (2)	1.18 (2)	1.11 (2)	2.50 (19)
BD-2	0.750 (2)	1.495 (2)	340 (7)	0.32 (1)	2.53 (2)	0.16 (1)	1.11 (2)	154 (2)	1.21 (2)	1.20 (2)	8.72 (31)
BD-3	0.751 (2)	1.501 (2)	499 (10)	0.33 (1)	3.75 (4)	0.16 (1)	1.48 (2)	156 (2)	1.23 (2)	1.29 (2)	18.07 (76)
TD-1	0.751 (2)	1.496 (2)	268 (5)	0.44 (1)	1.98 (1)	0.16 (1)	1.38 (2)	174 (2)	1.37 (2)	1.35 (2)	9.13 (30)
TD-2	0.747 (2)	1.498 (2)	348 (7)	0.46 (1)	2.58 (2)	0.15 (1)	1.50 (2)	173 (2)	1.37 (2)	1.39 (2)	14.75 (37)
TD-3	0.752 (2)	1.500 (2)	498 (10)	0.45 (1)	3.74 (4)	0.16 (1)	1.73 (3)	179 (2)	1.41 (2)	1.53 (2)	39.32 (98)



**Fig. 9.** Tomography images for shots BD-1 and TD-1. For XCT characterizations,  $x_1$ ,  $x_2$  and  $x_3$  represents LD, BD and TD, respectively for shot BD-1, and LD, TD and BD, respectively for shot TD-1.

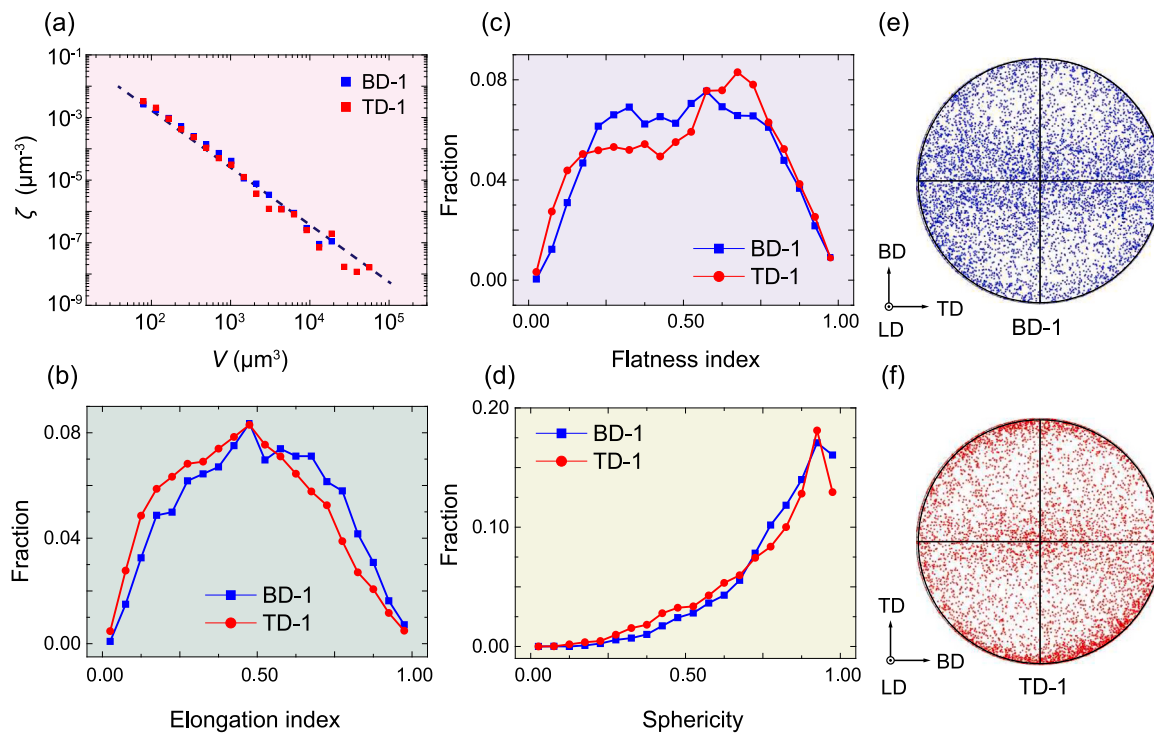


**Fig. 10.** Statistical analysis of void/crack topology. (a) Volume, (b) elongation index (EI), (c) flatness index (FI), (d) sphericity distributions of voids/cracks for shots BD-1 or TD-1. (e) and (f) Pole figures of the longest principal axis of voids/cracks for shots BD-1 or TD-1, respectively. The dashed line in (a) is linear fitting.

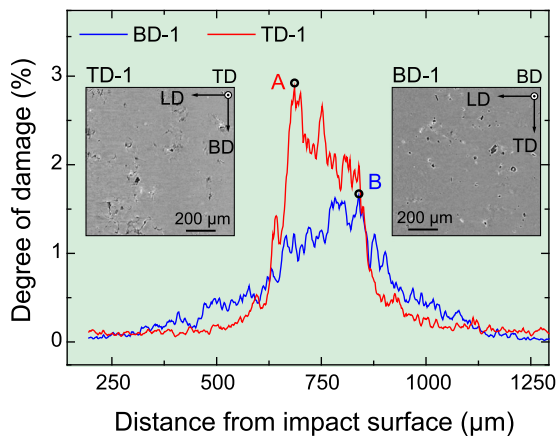


**Fig. 11.** Degree of damage as a function of distance away from the impact surface for shots BD-1 and TD-1. Insets are the tomogram slices with the maximum degree of damage on the LD-TD and LD-BD planes for shots BD-1 or TD-1, respectively.

$\dot{u}_1$  (deceleration upon release) is the absolute value of the slope of the release stage (DE), and

$$\dot{u}_1 = -\frac{du_{fs}(t)}{dt} \Big|_{DE}. \quad (7)$$

Similarly,  $\dot{u}_2$  (re-acceleration) which reflects the fracture rate during spallation [68] can be obtained as the slope of the rebound stage (EF),

$$\dot{u}_2 = \frac{du_{fs}(t)}{dt} \Big|_{EF}. \quad (8)$$

Moreover, the tensile strain rate can be estimated as [69,70]

$$\dot{\epsilon} \approx \frac{\dot{u}_1}{2C_B}. \quad (9)$$

The experimental parameters and results of all the six shots are summarized in [Table 2](#). The measured  $\sigma_{HEL}$  and  $\sigma_{sp}$  results agree with those reported by previous studies [45,46]. Due to the elastic wave decay along the shock direction [46,71], the  $\sigma_{HEL}$  value in this study is considerably smaller than that for thin samples ( $\sim 500 \mu\text{m}$ ) subjected to laser shock loading [47]. Different from the rolled dual-phase Ti alloy [72], textured Mg alloy [73], duplex stainless steel [74], CNT/2024Al composite [75] and previous studies on L-PBF-fabricated AlSi10Mg [45–47], the anisotropy in  $\sigma_{HEL}$  in this study is significant. Generally, the [111] orientation has the largest  $\sigma_{HEL}$  in the single crystal Al, followed closely by [110] and [100] [76]. Thus, as a result of the initial  $\langle 100 \rangle \parallel BD$  texture, the TD samples show higher  $\sigma_{HEL}$  than the BD samples.  $\sigma_{sp}$  for the TD samples is  $\sim 18\%$  higher than that for the BD sample. The related mechanism will be discussed below in conjunction with damage characterization.

### 3.2. Damage characterizations

The postmortem samples of shots BD-1, BD-2, TD-1 and TD-2 are sectioned along the dashed lines in [Fig. 5c](#), and their TD-BD planes are characterized with metallographic microscopy or SEM ([Fig. 7](#)). All spall damage features (voids or cracks) appear in the middle of the cross-sections given the flyer plate and sample dimensions [62]. Moreover, the damage within BD samples distributes over a wider range. The MPBs normally suffer from incomplete melting, are rich in flaws such as pores and inclusions, and have high microstructure inhomogeneity [77–79], and consequently, provide more low-barrier nucleation sites for voids [47]. Thus, almost all voids are located around the MPBs in [Fig. 7a](#). As shown in [Fig. 8](#), EBSD characterizations of two typical spallation regions for shot BD-1 prove that voids nucleate preferentially at MPBs, seconded by grain boundaries (GBs) within the pool interior.

In shot TD-1, several slender cracks propagate along BD in addition to isolated voids ([Fig. 7b](#)); the high KAM values regions extended along the BD direction due to the L-PBF fabrication process may ([Fig. 3g](#)) facilitate the formation of these slender cracks. For both loading directions, spall damage increases with increasing  $\sigma_H$ . Moreover, damage evolution shows significant anisotropy. For the BD samples, cracks propagate along the MPBs ([Fig. 7c](#)). However, for the TD samples, the cracks tend to propagate across the melt pools ([Fig. 7d](#)). Vastly different interpool and intrapool fracture modes [47] are found for loading along BD and TD, respectively.

Besides the metallographic microscopy characterization, synchrotron XCT is also conducted on postmortem samples of shots BD-1 and TD-1 to resolve the internal 3D damage characteristics. Their spatial distributions of voids or cracks within a sampling volume of  $1050 \times 1050 \times 1050 \mu\text{m}^3$  are shown in [Fig. 9a](#) and b. Consistent with the metallographic results ([Fig. 7](#)), voids are predominant for both shots ([Fig. 9e and f](#)), and a certain number of cracks extended on the BD-LD plane are identified for shot TD-1 ([Fig. 9f](#)).

The 3D configurations of the microvoids and cracks are segmented and then analyzed. Via the binning procedure [80], the volume distribution of voids or cracks is characterized in terms of probability density ( $\zeta$ ),

$$\zeta = \frac{1}{\lambda^k} \frac{\sum_{\lambda^{k-1} \leq V \leq \lambda^k-1} N(V)}{\sum N(V)}, \quad (10)$$

where  $N(V)$  is the number of cracks within the bin centered at volume  $V$ .  $\lambda$  is the binning width ( $1.4 \mu\text{m}^3$ ) and  $k$  denotes the sequence number of a bin. The  $\zeta - V$  distributions for the two shots are consistent ([Fig. 10a](#)) and can be described with the same power-law function,  $\zeta \approx V^{-1.32}$  (marked by the dashed line in [Fig. 10a](#)), indicating similar nucleation and growth dynamics for both shots [75].

Gyration tensor [50] is used to characterize the topology of void/crack networks, and defined in terms of the 3D voxel coordinates as

$$G_{\alpha\beta}^{(\omega)} = \frac{1}{V^{(\omega)}} \sum_{i=1}^{V^{(\omega)}} \left( x_{\alpha_i}^{(\omega)} - x_{\alpha_c}^{(\omega)} \right) \left( x_{\beta_i}^{(\omega)} - x_{\beta_c}^{(\omega)} \right). \quad (11)$$

For void or crack  $\omega$ ,  $V^{(\omega)}$  is the total number of voxels within the void/crack (i.e., void volume), and  $x_{\alpha_i}^{(\omega)}$  or  $x_{\beta_i}^{(\omega)}$  is the  $\alpha$  or  $\beta$  coordinate of voxel  $i$ . Here  $\alpha, \beta = 1, 2, 3$ , corresponding to  $x_1, x_2$  and  $x_3$ , respectively. Similarly,  $x_{\alpha_c}^{(\omega)}$  or  $x_{\beta_c}^{(\omega)}$  is the  $\alpha$  or  $\beta$  coordinate of the center of mass (c) of void  $\omega$ .

The eigenvalues of the gyration tensor are calculated as  $L_1, L_2$  and  $L_3$  ( $L_1 > L_2 > L_3$ ). Given the eigenvalues, a characteristic ellipsoid can be constructed for the crack with three semi-axes oriented along the eigenvectors, and their lengths are  $a_1 = \sqrt{5L_1}$ ,  $a_2 = \sqrt{5L_2}$  and  $a_3 = \sqrt{5L_3}$ . Furthermore, the sphericity ( $S_G$ ) can be defined as

$$S_G = 1 - \frac{1}{2} \frac{\sum_{i>j}^3 (L_i - L_j)^2}{\left( \sum_i^3 L_i \right)^2}, \quad (12)$$

where  $i, j = 1, 2, 3$ . Two aspect ratios, the elongation index (EI) and the flatness index (FI), can be calculated as

$$EI = \frac{L_2}{L_1}, \quad (13)$$

$$FI = \frac{L_3}{L_2}. \quad (14)$$

A smaller EI or FI means a greater degree of elongation or flatness.

For both shots BD-1 and TD-1, the distributions of EI ([Fig. 10b](#)), FI ([Fig. 10c](#)) and  $S_G$  ([Fig. 10d](#)) of void/crack networks are similar. The EI and FI distributions are bell-shaped, and the EI and FI values concentrate in the plateau region. The fraction of voids/cracks increases with increasing  $S_G$  ([Fig. 10d](#)). Given the existence of a certain number of cracks for shot TD-1, the fractions of voids/cracks in the low ranges of EI (0–0.3), FI (0–0.2) and  $S_G$  (0–0.4) for shot TD-1 are higher than those for shot BD-1.

Stereo graphic projection is used to project void/crack orientations onto a pole figure [81]. Since the tensile stress component along the impact direction is maximum for shot TD-1, the majority of isolated voids are prone to elongate along TD (Fig. 10f). However, some voids in shot BD-1 start to coalesce with each other (the blue arrows in Fig. 9e) to form cracks in XCT, and therefore, most of such coalesced voids (cracks) are perpendicular to the impact direction (Fig. 10e).

The degree of damage  $\xi$  is defined as

$$\xi = \frac{S_{\text{damage}}}{S_{\text{total}}}, \quad (15)$$

where  $S_{\text{damage}}$  and  $S_{\text{total}}$  are, respectively, damage area and total area for a tomogram slice perpendicular to the shock direction at a certain distance away from the impact surface. As shown in Fig. 11, main damage ( $\xi_{\text{max}}$ ) occurs in the distance range of 625–875 μm. Although the number of voids/cracks in shot BD-1 (3371 voids/cracks) is larger than that of shot TD-1 (2168 voids/cracks), shot TD-1 shows a higher  $\xi_{\text{max}}$  value, which is consistent with the higher fracture rate ( $\dot{\epsilon}_2$  in Fig. 6).

#### 4. Discussions

According to the self-consistent theory of spall fracture, the critical stress of void nucleation is approximately proportional to yield stress [82–84]. Thus, with lower dynamic yield stress and then low critical stress of void nucleation, the damage occurs over a wide range, then multiple spall planes appear for BD samples, in contrast with the concentrated damage distributed over a narrow range for TD samples. Since most of the energy is dissipated during the void nucleation process, then the damage evolution is insufficient, leading to the less  $\xi_{\text{max}}$  value for BD samples (Fig. 11). The TD samples show typical “brittle” behavior. Like brittle materials such as ceramics [85], once the voids nucleate, the damage propagates rapidly, resulting in the higher  $\xi_{\text{max}}$  value.

Based on the characterizations above, dissymmetric fish-scale-shaped melt pools are with convex contours opposite to the building direction, and coarse columnar grains in melt pool interior elongate also along BD, in other words, less GB number density along BD. Both the MPBs [77] and grain boundaries (GBs) [86] within the pool interior can act as weak zones for void nucleation (Fig. 8). Thus, there exists a competition mechanism between MPBs and GBs. When loading along BD, the spall plane coincides with more MPBs but less GBs within the pool interior. Almost all voids are located around the MPBs, indicating MPBs are the lower barrier nucleation sites (Fig. 8). When spall damage increases, the voids on the MPBs coalesce with each other, leading to the interpool fracture. For TD samples, given the higher GB density in the pool interior, some voids can also nucleate at GBs inside melt pools besides along the MPBs as spall damage increases. Then voids coalesce with each other and propagate across the melt pools, resulting in the intrapool fracture.

Moreover, due to the insufficient energy density [87] and poor overlap of melt pools (scan tracks) [88], lack of fusion defects, especially lack of fusion pores exist in L-PBF fabricated AlSi10Mg. Unlike the gas pores, lack of fusion pores exhibit preferred orientations [89], generally flat lack of fusion defects perpendicular to BD. These lack of fusion defects could lead to the anisotropy in ductility and fatigue life. The preferred orientations of the lack of fusion defects lead to higher stress concentrations at defects, then promote earlier fracture [90] or fatigue crack initiation [89,91] when loading along BD. These lack of fusion defects may act as nucleation sites, leading to lower spall strength for BD samples due to the defects preferred orientations. However, different from the MPBs and GBs, no direct observation of lack of fusion defects are characterized in this study. The role of lack of fusion defects deserve further investigations.

Overall, three orientation-dependent factors can be responsible for the spall strength and damage evolution: dynamic yield stress, the projected area of MPBs, and the GB number density in melt pool interior

along the loading direction. Moreover, voids nucleate preferentially at MPBs, seconded by GBs within the pool interior, thus TD samples owns less nucleation sites due to the less projected area of MPBs along the impact direction. In conclusion, less nucleation sites and higher yield stress lead to higher spall strength in the TD samples.

For body-centered cubic additive manufactured alloys such as 24Cr NiMo steel [92] and tantalum [93], the transgranular cleavage (24CrNiMo steel) or intergranular cracking (tantalum) within the melt pool is brittle in nature, thus their activation does not require substantial plastic deformation in contrast to cracking along MPBs. Moreover, the fraction of MPBs is considerably smaller than those of cleavage planes and GBs. Therefore, the MPBs show negligible influence on fracture of them.

Different from the L-PBF-fabricated AlSi10Mg in this study, previous publications indicated negligible anisotropy in spall strength [45–47]. A probable reason is a degree of porosity from fabrication process in AlSi10Mg. The pre-existing voids will weaken the effects of structural anisotropy. Our previous plate impact experiments on 5% porosity aluminum showed that instead of nucleation of new voids, the spallation voids were generated via growth of pre-existing voids [94].

#### 5. Conclusions

The L-PBF-fabricated AlSi10Mg is subjected to plate impact loading along BD and TD. Free-surface velocity history measurements, and postmortem metallographic and XCT characterizations are conducted. Our main conclusions are as follows.

- The L-PBF-fabricated AlSi10Mg exhibits an anisotropic microstructure: fish-scale-shaped melt pools overlaid along the building direction, coarser columnar grains elongated along ⟨100⟩ in the melt pool interior (thus, the GB number density shows anisotropy), and finer equiaxed grains at MPBs.
- The microstructural anisotropy of L-PBF-fabricated AlSi10Mg induces an anisotropy in HEL and spall strength. The HEL and spall strength for loading along TD are about 40% and 18% higher than those along BD, respectively.
- Voids nucleate preferentially at MPBs, seconded by GBs within the pool interior. Spall strength and damage evolution are combined results of three orientation-dependent factors: dynamic yield stress, the projected area of MPBs, and the GB number density in melt pool interior along the loading direction.
- The higher yield stress and less projected area of MPBs along the impact direction lead to higher spall strength in the TD samples, but the damage is more “brittle” and manifested as interpool damage given the higher GB density in the pool interior and lower projected area of MPBs.
- The weaker MPBs and the larger projected area of MPBs lead to easier and broader nucleation of voids, leading to wider, more “ductile”, interpool damage in the BD samples.

#### CRediT authorship contribution statement

**N.B. Zhang:** Conceptualization, Investigation, Methodology, Writing – original draft. **K. Yang:** Investigation, Methodology. **Y.C. Li:** Visualization. **Z.H. Lin:** Methodology. **Y. Cai:** Resources. **H.W. Chai:** Investigation, Visualization, Data curation. **H.L. Xie:** Resources. **L. Lu:** Validation, Supervision. **S.N. Luo:** Validation, Supervision, Writing – review & editing, Project administration, Funding acquisition, Resources.

#### Declaration of competing interest

The authors declare that they have no known competing financial interests or personal relationships that could have appeared to influence the work reported in this paper.

## Data availability

Data will be made available on request.

## Acknowledgments

This work was sponsored in part by Sichuan Science and Technology Program (Grant Nos. 2022YFG0033, 2022YFG0365) and Natural Science Foundation of China (Grant Nos. 12302489, 12102491 and 11627901).

## References

- [1] W.J. Sames, F. List, S. Pannala, R.R. Dehoff, S.S. Babu, The metallurgy and processing science of metal additive manufacturing, *Int. Mater. Rev.* 61 (5) (2016) 315–360.
- [2] W.E. Frazier, Metal additive manufacturing: a review, *J. Mater. Eng. Perform.* 23 (2014) 1917–1928.
- [3] H. Bikas, P. Stavropoulos, G. Chryssolouris, Additive manufacturing methods and modelling approaches: a critical review, *Int. J. Adv. Manuf. Technol.* 83 (2016) 389–405.
- [4] J.J. Lewandowski, M. Seifi, Metal additive manufacturing: a review of mechanical properties, *Annu. Rev. Mater. Res.* 46 (2016) 151–186.
- [5] D.D. Gu, W. Meiners, K. Wissenbach, R. Poprawe, Laser additive manufacturing of metallic components: materials, processes and mechanisms, *Int. Mater. Rev.* 57 (3) (2012) 133–164.
- [6] J.H. Martin, B.D. Yahata, J.M. Hundley, J.A. Mayer, T.A. Schaedler, T.M. Pollock, 3D printing of high-strength aluminium alloys, *Nature* 549 (7672) (2017) 365–369.
- [7] B. Chen, S. Moon, X. Yao, G. Bi, J. Shen, J. Umeda, K. Kondoh, Strength and strain hardening of a selective laser melted AlSi10Mg alloy, *Scr. Mater.* 141 (2017) 45–49.
- [8] K.V. Yang, Y. Shi, F. Palm, X. Wu, P. Rometsch, Columnar to equiaxed transition in Al-Mg-(Sc)-Zr alloys produced by selective laser melting, *Scr. Mater.* 145 (2018) 113–117.
- [9] E. Louvis, P. Fox, C.J. Sutcliffe, Selective laser melting of aluminium components, *J. Mater. Process. Technol.* 211 (2) (2011) 275–284.
- [10] N. Read, W. Wang, K. Essa, M.M. Attallah, Selective laser melting of AlSi10Mg alloy: Process optimisation and mechanical properties development, *Mater. Des.* 65 (2015) 417–424.
- [11] W. Li, S. Li, J. Liu, A. Zhang, Y. Zhou, Q. Wei, C. Yan, Y. Shi, Effect of heat treatment on AlSi10Mg alloy fabricated by selective laser melting: Microstructure evolution, mechanical properties and fracture mechanism, *Mater. Sci. Eng. A* 663 (2016) 116–125.
- [12] A. Hadadzadeh, B.S. Amirkhiz, A. Oodeshi, M. Mohammadi, Dynamic loading of direct metal laser sintered AlSi10Mg alloy: Strengthening behavior in different building directions, *Mater. Des.* 159 (2018) 201–211.
- [13] M.L. Montero-Sistiaga, R. Mertens, B. Vrancken, X. Wang, B. Van Hooreweder, J.-P. Kruth, J. Van Humbeeck, Changing the alloy composition of Al7075 for better processability by selective laser melting, *J. Mater. Process. Technol.* 238 (2018) 437–445.
- [14] H. Xia, Q. Sun, S. Wang, Influence of strain rate effect on energy absorption characteristics of bio-inspired honeycomb column thin-walled structure under impact loading, *Case Stud. Constr. Mat.* 18 (2023) e01761.
- [15] S. Xu, Q. Lu, Y. Ou, P. Zhang, H. Yan, T. Sun, S. Ma, Z. Luo, Y. Tian, Effect of heat treatment on the anisotropic mechanical properties of AlSi10Mg fabricated by selective laser melting, *J. Mater. Eng. Perform.* (2023) 1–14.
- [16] Z. Wu, S. Wu, X. Gao, Y. Lin, Y. Xue, P.J. Withers, The role of internal defects on anisotropic tensile failure of L-PBF AlSi10Mg alloys, *Sci. Rep.* 13 (1) (2023) 14681.
- [17] S. Wang, J. Ning, L. Zhu, Z. Yang, W. Yan, Y. Dun, P. Xue, P. Xu, S. Bose, A. Bandyopadhyay, Role of porosity defects in metal 3D printing: Formation mechanisms, impacts on properties and mitigation strategies, *Mater. Today*.
- [18] Q.C. Johnson, C.M. Laursen, A.D. Spear, J.D. Carroll, P.J. Noell, Analysis of the interdependent relationship between porosity, deformation, and crack growth during compression loading of LPBF AlSi10Mg, *Mater. Sci. Eng. A* 852 (2022) 143640.
- [19] L. Zhao, L. Song, J.G.S. Macías, Y. Zhu, M. Huang, A. Simar, Z. Li, Review on the correlation between microstructure and mechanical performance for laser powder bed fusion AlSi10Mg, *Addit. Manuf.* 56 (2022) 102914.
- [20] F. Sausto, P. Carrion, N. Shamsaei, S. Beretta, Fatigue failure mechanisms for AlSi10Mg manufactured by L-PBF under axial and torsional loads: The role of defects and residual stresses, *Int. J. Fatigue* 162 (2022) 106903.
- [21] J. Delahaye, J.T. Tchuindjang, J. Lecomte-Beckers, O. Rigo, A. Habraken, A. Mertens, Influence of Si precipitates on fracture mechanisms of AlSi10Mg parts processed by selective laser melting, *Acta Mater.* 175 (2019) 160–170.
- [22] K. Kempen, L. Thijss, J. Van Humbeeck, J.-P. Kruth, Mechanical properties of AlSi10Mg produced by selective laser melting, *Phys. Procedia* 39 (2012) 439–446.
- [23] I. Rosenthal, A. Stern, N. Frage, Strain rate sensitivity and fracture mechanism of AlSi10Mg parts produced by selective laser melting, *Mater. Sci. Eng. A* 682 (2017) 509–517.
- [24] N.E. Uzan, R. Shneck, O. Yeheskel, N. Frage, High-temperature mechanical properties of AlSi10Mg specimens fabricated by additive manufacturing using selective laser melting technologies (AM-SLM), *Addit. Manuf.* 24 (2018) 257–263.
- [25] N.T. Aboulkhair, I. Maskery, C. Tuck, I. Ashcroft, N.M. Everett, The microstructure and mechanical properties of selectively laser melted AlSi10Mg: The effect of a conventional T6-like heat treatment, *Mater. Sci. Eng. A* 667 (2016) 139–146.
- [26] C. Biffi, J. Fiocchi, P. Bassani, A. Tuissi, Continuous wave vs pulsed wave laser emission in selective laser melting of AlSi10Mg parts with industrial optimized process parameters: Microstructure and mechanical behaviour, *Addit. Manuf.* 24 (2018) 639–646.
- [27] L. Hitzler, N. Schoch, B. Heine, M. Merkel, W. Hall, A. Öchsner, Compressive behaviour of additively manufactured AlSi10Mg: Druckeigenschaften additiv gefertigter AlSi10Mg proben, *Mater.wiss. Werkst.tech.* 49 (5) (2018) 683–688.
- [28] M. Schuch, T. Hahn, M. Bleckmann, The mechanical behavior and microstructure of additively manufactured AlSi10Mg for different material states and loading conditions, *Mater. Sci. Eng. A* 813 (2021) 141134.
- [29] B. Amir, E. Kochavi, S. Gruntman, Y. Gale, S. Samuha, O. Sadot, Experimental investigation on shear strength of laser powder bed fusion AlSi10Mg under quasi-static and dynamic loads, *Addit. Manuf.* 46 (2021) 102150.
- [30] L. Thijss, K. Kempen, J.-P. Kruth, J. Van Humbeeck, Fine-structured aluminium products with controllable texture by selective laser melting of pre-alloyed AlSi10Mg powder, *Acta Mater.* 61 (5) (2013) 1809–1819.
- [31] P. Delroisse, P.J. Jacques, E. Maire, O. Rigo, A. Simar, Effect of strut orientation on the microstructure heterogeneities in AlSi10Mg lattices processed by selective laser melting, *Scr. Mater.* 141 (2017) 32–35.
- [32] T. Maconachie, M. Leary, J. Zhang, A. Medvedev, A. Sarker, D. Ruan, G. Lu, O. Farouque, M. Brandt, Effect of build orientation on the quasi-static and dynamic response of SLM AlSi10Mg, *Mater. Sci. Eng. A* 788 (2020) 139445.
- [33] M.J. Paul, Q. Liu, J.P. Best, X. Li, J.J. Kružić, U. Ramamurthy, B. Gludovatz, Fracture resistance of AlSi10Mg fabricated by laser powder bed fusion, *Acta Mater.* 211 (2021) 116869.
- [34] T.D. Piette, R.J. Warren, A.G. Spangenberg, E.J. Hummelt, D.A. Lados, Microstructure evolution, fatigue crack growth, and ultrasonic fatigue in as-fabricated laser powder bed and conventionally cast Al-10Si-0.4Mg: a mechanistic understanding and integrated flaw-sensitive fatigue design methods, *Mater. Sci. Eng. A* 825 (2021) 141892.
- [35] N. Takata, H. Kodaira, K. Sekizawa, A. Suzuki, M. Kobashi, Change in microstructure of selectively laser melted AlSi10Mg alloy with heat treatments, *Mater. Sci. Eng. A* 704 (2017) 218–228.
- [36] X. Liu, C. Zhao, X. Zhou, Z. Shen, W. Liu, Microstructure of selective laser melted AlSi10Mg alloy, *Mater. Des.* 168 (2019) 107677.
- [37] X. Li, D. Yi, X. Wu, J. Zhang, X. Yang, Z. Zhao, Y. Feng, J. Wang, P. Bai, B. Liu, et al., Effect of construction angles on microstructure and mechanical properties of AlSi10Mg alloy fabricated by selective laser melting, *J. Alloys Compd.* 881 (2021) 160459.
- [38] B. Amir, S. Samuha, O. Sadot, Influence of selective laser melting machine source on the dynamic properties of AlSi10Mg alloy, *Materials* 12 (7) (2019) 1143.
- [39] H. Asgari, A. Oodeshi, K. Hosseinkhani, M. Mohammadi, On dynamic mechanical behavior of additively manufactured AlSi10Mg\_200C, *Mater. Lett.* 211 (2018) 187–190.
- [40] A. Hadadzadeh, B.S. Amirkhiz, A. Oodeshi, J. Li, M. Mohammadi, Role of hierarchical microstructure of additively manufactured AlSi10Mg on dynamic loading behavior, *Addit. Manuf.* 28 (2019) 1–13.
- [41] B. Nurel, M. Nahmany, N. Frage, A. Stern, O. Sadot, Split hopkinson pressure bar tests for investigating dynamic properties of additively manufactured AlSi10Mg alloy by selective laser melting, *Addit. Manuf.* 22 (2018) 823–833.
- [42] P. Ponnusamy, S. Masood, D. Ruan, S. Palanisamy, R.R. Rashid, R. Mukhlis, N.J. Edwards, Dynamic compressive behaviour of selective laser melted AlSi12 alloy: Effect of elevated temperature and heat treatment, *Addit. Manuf.* 36 (2020) 101614.
- [43] C. Baxter, E. Cyr, A. Oodeshi, M. Mohammadi, Constitutive models for the dynamic behaviour of direct metal laser sintered AlSi10Mg\_200C under high strain rate shock loading, *Mater. Sci. Eng. A* 731 (2018) 296–308.
- [44] B. Amir, E. Grinberg, Y. Gale, O. Sadot, S. Samuha, Influences of platform heating and post-processing stress relief treatment on the mechanical properties and microstructure of selective-laser-melted AlSi10Mg alloys, *Mater. Sci. Eng. A* 822 (2021) 141612.
- [45] P.E. Specht, N.P. Brown, Shock compression response of additively manufactured AlSi10Mg, *J. Appl. Phys.* 130 (24) (2021) 245104.
- [46] E. Zaretsky, A. Stern, N. Frage, Dynamic response of AlSi10Mg alloy fabricated by selective laser melting, *Mater. Sci. Eng. A* 688 (2017) 364–370.
- [47] M. Laurençon, T. De Resegue, D. Loison, J. Baillargeat, J.D. Ngnekou, Y. Nadot, Effects of additive manufacturing on the dynamic response of AlSi10Mg to laser shock loading, *Mater. Sci. Eng. A* 748 (2019) 407–417.

- [48] P.F. Zhang, W. Zhou, H.F. Yin, Y.J. Shang, Progressive damage analysis of three-dimensional braided composites under flexural load by micro-CT and acoustic emission, *Compos. Struct.* 226 (2019) 111196.
- [49] L. Geng, W. Wu, L. Sun, D. Fang, Damage characterizations and simulation of selective laser melting fabricated 3D re-entrant lattices based on in-situ CT testing and geometric reconstruction, *Int. J. Mech. Sci.* 157 (2019) 231–242.
- [50] H.W. Chai, Z.L. Xie, X.H. Xiao, H.L. Xie, J.Y. Huang, S.N. Luo, Microstructural characterization and constitutive modeling of deformation of closed-cell foams based on in situ X-ray tomography, *Int. J. Plast.* 131 (2020) 102730.
- [51] Q. Yan, B. Song, Y. Shi, Comparative study of performance comparison of AlSi10Mg alloy prepared by selective laser melting and casting, *J. Mater. Sci. Technol.* 41 (2020) 199–208.
- [52] G. Karthik, H.S. Kim, Heterogeneous aspects of additive manufactured metallic parts: a review, *Met. Mater. Int.* 27 (2021) 1–39.
- [53] J.D. Verhoeven, Fundamentals of Physical Metallurgy, John Wiley & Sons Incorporated, 1975.
- [54] M. Fousová, D. Dvorský, A. Michalcová, D. Vojtěch, Changes in the microstructure and mechanical properties of additively manufactured AlSi10Mg alloy after exposure to elevated temperatures, *Mater. Charact.* 137 (2018) 119–126.
- [55] Y. Bai, Y. Yang, Z. Xiao, M. Zhang, D. Wang, Process optimization and mechanical property evolution of AlSiMg0.75 by selective laser melting, *Mater. Des.* 140 (2018) 257–266.
- [56] J.M. Brown, R.G. McQueen, Phase transitions, Grüneisen parameter, And elasticity for shocked iron between 77 GPa and 400 GPa, *J. Geophys. Res.-Sol. Ea.* 91 (B7) (1986) 7485–7494.
- [57] N. Bourne, G. Gray, Computational design of recovery experiments for ductile metals, *Proc. R. Soc. A.* 461 (2002) (2005) 3297–3312.
- [58] R. Vignjević, K. Hughes, T. De Vuyst, N. Djordjević, J.C. Campbell, M. Stojković, O. Gulavani, S. Hiermaier, Lagrangian analysis led design of a shock recovery plate impact experiment, *Int. J. Impact Eng.* 77 (2015) 16–29.
- [59] O.T. Strand, D. Goosman, C. Martinez, T. Whitworth, W. Kuhlow, Compact system for high-speed velocimetry using heterodyne techniques, *Rev. Sci. Instrum.* 77 (8) (2006) 083108.
- [60] D. Dolan, Accuracy and precision in photonic doppler velocimetry, *Rev. Sci. Instrum.* 81 (5) (2010) 053905.
- [61] Y. Li, X. Zhou, C. Liu, S.N. Luo, Refractive indices of CaF<sub>2</sub> single crystals under elastic shock loading, *J. Appl. Phys.* 122 (4).
- [62] N.B. Zhang, Q. Liu, K. Yang, C. Li, Y. Cai, S.N. Luo, X.H. Yao, S. Chen, Effects of shock-induced phase transition on spallation of a mild carbon steel, *Int. J. Mech. Sci.* 213 (2022) 106858.
- [63] L. Davison, Fundamentals of Shock Wave Propagation in Solids, Springer Science & Business Media, 2008.
- [64] S.P. Marsh, LASL Shock Hugoniot Data, Vol. 5, Univ of California Press, 1980.
- [65] G. Stepanov, Spall fracture of metals by elastic-plastic loading waves, *Prob. Strength (USSR)* 8 (1976) 66–70.
- [66] V. Romanchenko, G. Stepanov, Dependence of the critical stresses on the loading time parameters during spall in copper, aluminum, and steel, *J. Appl. Mech. Tech. Phys.* 21 (4) (1980) 555–561.
- [67] T. Antoun, D.R. Curran, L. Seaman, G.I. Kanel, S.V. Razorenov, A.V. Utkin, Spall Fracture, Springer Science & Business Media, New York, 2003.
- [68] G.I. Kanel, A.V. Utkin, Estimation of the spall fracture kinetics from the free-surface velocity profiles, in: AIP Conf. Proc., Vol. 370, AIP, Seattle, Washington (USA), 1996, pp. 487–490.
- [69] G.I. Kanel, Spall fracture: methodological aspects, mechanisms and governing factors, *Int. J. Fract.* 163 (1–2) (2010) 173–191.
- [70] B. Arman, S.N. Luo, T.C. Germann, T. Çağın, Dynamic response of Cu46Zr54 metallic glass to high-strain-rate shock loading: plasticity, spall, and atomic-level structures, *Phys. Rev. B* 81 (14) (2010) 144201.
- [71] J.P. Billingsley, The decay limit of the hugoniot elastic limit, *Int. J. Impact Eng.* 21 (4) (1998) 267–281.
- [72] J. Tan, L. Lu, H.Y. Li, X.H. Xiao, Z. Li, S.N. Luo, Anisotropic deformation and damage of dual-phase Ti-6Al-4V under high strain rate loading, *Mater. Sci. Eng. A* 742 (2019) 532–539.
- [73] Z.H. Dai, L. Lu, H.W. Chai, X.H. Xiao, X.L. Gong, S.N. Luo, Mechanical properties and fracture behavior of Mg-3Al-1Zn alloy under high strain rate loading, *Mater. Sci. Eng. A* 789 (2020) 139690.
- [74] C. Li, J. Huang, X. Tang, H. Chai, X. Xiao, Z. Feng, S.N. Luo, Effects of structural anisotropy on deformation and damage of a duplex stainless steel under high strain rate loading, *Mater. Sci. Eng. A* 705 (2017) 265–272.
- [75] J.C. Cheng, H.W. Chai, G.L. Fan, Z.Q. Li, H.L. Xie, Z.Q. Tan, B.X. Bie, J.Y. Huang, S.N. Luo, Anisotropic spall behavior of CNT/2024Al composites under plate impact, *Carbon* 170 (2020) 589–599.
- [76] G. Owen, D. Chapman, G. Whiteman, S. Stirk, J. Millett, S. Johnson, Spall behaviour of single crystal aluminium at three principal orientations, *J. Appl. Phys.* 122 (15) (2017) 155102.
- [77] S.R. Ch, A. Raja, R. Jayaganthan, N. Vasa, M. Raghuandan, Study on the fatigue behaviour of selective laser melted AlSi10Mg alloy, *Mater. Sci. Eng. A* 781 (2020) 139180.
- [78] Y. Sun, R.J. Hebert, M. Aindow, Non-metallic inclusions in 17-4PH stainless steel parts produced by selective laser melting, *Mater. Des.* 140 (2018) 153–162.
- [79] S. Huang, R.L. Narayan, J.H.K. Tan, S.L. Sing, W.Y. Yeong, Resolving the porosity-unmelted inclusion dilemma during in-situ alloying of Ti34Nb via laser powder bed fusion, *Acta Mater.* 204 (2021) 116522.
- [80] K. Joshi, A. Rav, A. Sur, T. Kaushik, S.C. Gupta, Spall fracture in aluminium alloy at high strain rates, in: AIP Conf. Proc. Vol. 1731, AIP Publishing LLC, 2016, 060013.
- [81] Y.L. Bian, Q. Liu, Z.D. Feng, J.Y. Hua, H.L. Xie, S. Chen, Y. Cai, X.H. Yao, S.N. Luo, High-speed penetration dynamics of polycarbonate, *Int. J. Mech. Sci.* 223 (2022) 107250.
- [82] Y. Huang, J. Hutchinson, V. Tvergaard, Cavitation instabilities in elastic-plastic solids, *J. Mech. Phys. Solids* 39 (2) (1991) 223–241.
- [83] T. Wright, K. Ramesh, Dynamic void nucleation and growth in solids: a self-consistent statistical theory, *J. Mech. Phys. Solids* 56 (2) (2008) 336–359.
- [84] J. Wilkerson, On the micromechanics of void dynamics at extreme rates, *Int. J. Plast.* 95 (2017) 21–42.
- [85] G. Raiser, J. Wise, R. Clifton, D. Grady, D. Cox, Plate impact response of ceramics and glasses, *J. Appl. Phys.* 75 (8) (1994) 3862–3869.
- [86] J.W. Wilkerson, K.T. Ramesh, Unraveling the anomalous grain size dependence of cavitation, *Phys. Rev. Lett.* 117 (21) (2016) 215503.
- [87] K.V. Yang, P. Rometsch, T. Jarvis, J. Rao, S. Cao, C. Davies, X. Wu, Porosity formation mechanisms and fatigue response in Al-Si-Mg alloys made by selective laser melting, *Mater. Sci. Eng. A* 712 (2018) 166–174.
- [88] M. Tang, P.C. Pistorius, J.L. Beuth, Prediction of lack-of-fusion porosity for powder bed fusion, *Addit. Manuf.* 14 (2017) 39–48.
- [89] Z. Wu, S. Wu, J. Bao, W. Qian, S. Karabal, W. Sun, P.J. Withers, The effect of defect population on the anisotropic fatigue resistance of AlSi10Mg alloy fabricated by laser powder bed fusion, *Int. J. Fatigue* 151 (2021) 106317.
- [90] L. Zhao, J.G.S. Macias, L. Ding, H. Idrissi, A. Simar, Damage mechanisms in selective laser melted AlSi10Mg under as built and different post-treatment conditions, *Mater. Sci. Eng. A* 764 (2019) 138210.
- [91] N. Larrosa, W. Wang, N. Read, M. Loretto, C. Evans, J. Carr, U. Tradowsky, M. Attallah, P. Withers, Linking microstructure and processing defects to mechanical properties of selectively laser melted AlSi10Mg alloy, *Theor. Appl. Fract. Mech.* 98 (2018) 123–133.
- [92] K. Yang, Y. Chen, X. Liu, C. Li, H. Chen, J. Huang, S. Luo, Spall properties and damage mechanisms of a low-alloy steel fabricated via laser powder bed fusion, *Mater. Sci. Eng. A* 840 (2022) 142910.
- [93] D.R. Jones, S.J. Fensin, B.G. Ndefru, D.T. Martinez, C.P. Trujillo, G.T. Gray III, Spall fracture in additive manufactured tantalum, *J. Appl. Phys.* 124 (22) (2018) 225902.
- [94] Y. Yao, H.W. Chai, C. Li, B.X. Bie, X.H. Xiao, J.Y. Huang, M.L. Qi, S.N. Luo, Deformation and damage of sintered low-porosity aluminum under planar impact: microstructures and mechanisms, *J. Mater. Sci.* 53 (2018) 4582–4597.